Deep phenotyping of the prostate tumor microenvironment reveals molecular stratifiers of relapse and links inflammatory chemokine expression to aberrant metabolism

Sebastian Krossa[1,2], Maria K. Andersen[1,3], Elise Midtbust[1,3], Maximilian Wess[1], Antti Kiviaho[4], Abhibhav Sharma[5], Trond Viset[6], Øystein Størkersen[6], Guro F. Giskeødegård[5], Matti Nykter[4,7], Alfonso Urbanucci[4,8], Morten B. Rye[3,9], and May-Britt Tessem[1,3]

1. Department of Circulation and Medical Imaging, Norwegian University of Science and Technology
2. Central staff, St. Olavs Hospital HF, 7006, Trondheim, Norway
3. Clinic of Surgery, St. Olavs Hospital, Trondheim University Hospital, Trondheim, Norway
4. Prostate Cancer Research Center, Faculty of Medicine and Health Technology, Tampere University and TAYS Cancer Center, Tampere, Finland
5. HUNT Center for Molecular and Clinical Epidemiology, Department of Public Health and Nursing, Norwegian University of Science and Technology (NTNU), Trondheim, Norway
6. Department of Pathology, St. Olavs Hospital, Trondheim University Hospital, Trondheim, Norway
7. Foundation for the Finnish Cancer Institute, Helsinki, Finland
8. Department of Tumor Biology, Institute for Cancer Research, Oslo University Hospital, Oslo, Norway
9. Department of Clinical and Molecular Medicine, Norwegian University of Science and Technology

Abstract

Understanding the molecular characteristics and changes of the tumor microenvironment (TME) associated with aggressive prostate cancer (PCa) is essential for precise diagnosis and treatment. We interrogated spatially resolved integrated transcriptomics and metabolomics data to build molecular signatures capable of discriminating patients with aggressive, potentially relapsing, and metastasizing PCa. We report two signatures characterized by upregulated expression of immune response related genes with increased activity in relapsing patients. The signature *Relapse* was active in cancer, stroma, and glandular tissue while the other was a feature of morphologically normal appearing glands (NAG) adjacent to aggressive cancer and was named the NAG signature. The NAG signature scored high in regions with upregulated expression of pro-inflammatory chemokines and in glandular regions enriched with Club-like cells and immune cell infiltration in the surrounding stroma. Regions which scored high for both NAG and relapse were associated with loss of normal prostate secretory gland functions such as reduced expression of genes necessary for citrate secretion and reduced levels of citrate and zinc. Our findings suggest that aggressive PCa is associated with an increased inflammatory status linked to chemokine production and Club-like cells.

Introduction/Main

Prostate cancer (PCa) is the most common malignancy among men in western countries [1]. This disease is clinically, morphologically, and molecularly highly heterogeneous, which determines aggressiveness and clinical outcome [2]. Approximately 30% of PCa patients experience relapse and improvement of patient stratification based on an increasing number of clinical and molecular parameters is an ongoing effort [3]. In search for more predictive biomarkers, substantial efforts are put into analyzing human PCa tissue. Specifically, to capture the transcriptomic heterogeneity single-cell and more recently spatial transcriptomics (ST) have emerged as popular technologies to study

heterogenous PCa tissue samples[4-7]. ST has the advantage of capturing transcriptomics profiles in hundreds and thousands of positional coordinates across the tissue sample thus offering a unique possibility to study the transcriptome in the spatial context, including intra-tumor heterogeneity, tumor microenvironment (TME) interactions, immune infiltration, and tissue-morphology-specific expression. While single-cell transcriptomics has given new insight on cell-type specific transcriptome signatures present in the prostate [8, 9], combining ST with single-cell transcriptomics shows considerable potential, as it has revealed highly detailed information on tumor-immune interaction in the prostate TME [5].

Alongside transcriptomic, metabolomic changes are another important hallmark of cancer. One prominent and characteristic example for PCa is the pronounced reduction of citrate levels which are typically elevated in a healthy prostate [10, 11]. Our prior research has demonstrated that the diverse content of stroma can obscure the true differences of citrate, in addition to other metabolites and DNA transcripts, when comparing benign and PCa tissue samples [12]. This highlights the need for spatially resolved methodology integrating several -omics layers to gain an elevated understanding of PCa.

Here, we collected spatial transcriptomics, metabolomics, and detailed histopathology data from 32 prostate tissue samples to dissect the biology of the PCa TME. To isolate unique characteristics and markers of aggressive PCa we collected these samples from 5 patients experiencing post-radical prostatectomy cancer relapse with confirmed metastasis and from 3 patients remaining relapse-free for up to 10 years after surgery. For validation and evaluation of this spatially resolved data in a larger cohort, we collected bulk transcriptomics and metabolomics data from 37 patients including those 8 patients used to obtain the spatial-omics data. Interrogating the spatial data, we found two gene expression signatures with an elevated activity in relapsing patients. While the first signature captured changes in cancer, stroma, and glandular regions, the second was mainly active in histologically normal appearing glands and dominated by pro-inflammatory chemokines. We found that Club-like cells were enriched in and near these glands and are the likely source of these chemokines. Further, we show, that both signatures are linked to PCa-characteristic transcriptional and metabolic changes such as loss of luminal function, reduction of citrate levels and secretion, and an increased energy demand. Our approach allowed us to identify transcriptomic markers for highly localized metabolic aberrations in morphologically normal appearing glands in the TME of aggressive PCa highlighting the huge potential of integrating spatial-omics data to unravel the complexity and heterogeneity of cancer tissue.

Results & Discussion

Relapse and Normal Appearing Gland (NAG) signatures derived from spatial transcriptomics data

To explore the *in vivo* gene expression in its spatial, histology context we captured and analyzed spatially resolved RNA termed spatial transcriptomics (ST) in 19854 circular spots from 32 tissue samples from prostatectomies of 8 of the 37 PCa patients in this study (**Figure 1a**). Of the 8 patients, 5 experienced relapse and 3 remained relapse free during a follow-up of 10 years (**Table 1, Supplementary Table 1**). The 32 tissue samples were labeled according to sample location (Cancer, Field, or Normal core location) (**Figure 1a**). Each ST spot was assigned a histopathology class, which included Cancer with ISUP grade, non-cancerous glands (NCG), stroma, lymphocytes, lymphocyte enriched stroma and cancerous perineural invasion (PNI) (**Figure 1a, Methods**).

Each of the 32 samples was also subjected to multi-layered spatial analysis using mass spectrometry imaging (MSI) to obtain spatial metabolomics data and immunohistochemistry staining. Further, these 32 samples together with an additional 142 samples from the remaining 29 of the 37 PCa patients were subjected to bulk transcriptomic and metabolomic analysis using RNA sequencing and high-resolution magic-angle spinning (HRMAS) NMR (**Figure 1a**).

To investigate differences in the transcriptome between relapsing and non-relapsing patients, we first identified sets of genes for each the histopathology classes individually by using the ST data. The genes were selected based on highest expression variability and deregulation combined with gene ontology enrichment-based filtering. This approach revealed inflammatory processes as major difference between these patient groups through chemokine and chemokine related ontologies, such as chemokine activity, neutrophil chemotaxis, chemokine-mediated signaling pathways, and CXCR chemokine receptor binding. We thus decided to emphasize our focus on chemokines by manually including all chemokines detected in the ST data into our signature generation pipeline (see **Methods** and **Supplementary Figure 2b**). We found a set of 26 genes which were able to distinguish relapsed from non-relapsed patients across all histopathology classes (**Supplementary Figure S3**). We termed this set of genes the *Relapse* signature, which contained 18 genes with higher expression in relapsed patients, and 8 genes with higher expression in non-relapsed patients (**Figure 1b**).

Most of the upregulated genes (14/18) in the Relapse signature were directly related to immune response processes. In addition, we observed that the Relapse signature displayed transcriptome changes in some of the subregions histologically classified as NCG in samples, close and distant to the cancer alike, from relapse in contrast to non-relapsing patients (**Figure 2a,** Supplementary **Figure 2a & 3a**). We therefore derived a gene set particularly capturing the changes in these apparently aberrant NCGs in relapse patients. We termed this the Normal Appearing Gland signature (NAG signature), reflecting the fact that these glands displayed clear transcriptional differences despite appearing histologically normal.

*Table 1 Clinical data for all patients included in this study. The table is divided by patients of which tissue samples were used for spatial transcriptomics and bulk transcriptomics. All spatial transcriptomics samples were also analyzed with bulk transcriptomics. *For one patient T-stage information was not available.*

	Spatial Transcriptomics		Bulk Transcriptomics	
	Relapse (n=5)	Non-relapse (n=3)	Relapse (n=27)	Non-relapse (n=10)
Post surgery ISUP grade	ISUP2, n=1 ISUP3, n=1 ISUP4, n=1 ISUP5, n=2	ISUP2, n=2 ISUP3, n=1	ISUP2, n=7 ISUP3, n=10 ISUP4, n=4 ISUP5, n=6	ISUP2, n=8 ISUP3, n=2
Mean age at surgery	59	60.7	62.4	59.8
Mean preoperative PSA	23.7	14.0	18.7	10.8
Clinical T-stage*	T2c, n=1 T3a, n=2 T3b, n=2	T2c, n=2*	T2c, n=9 T3a, n=6 T3b, n=12	T2c, n=9

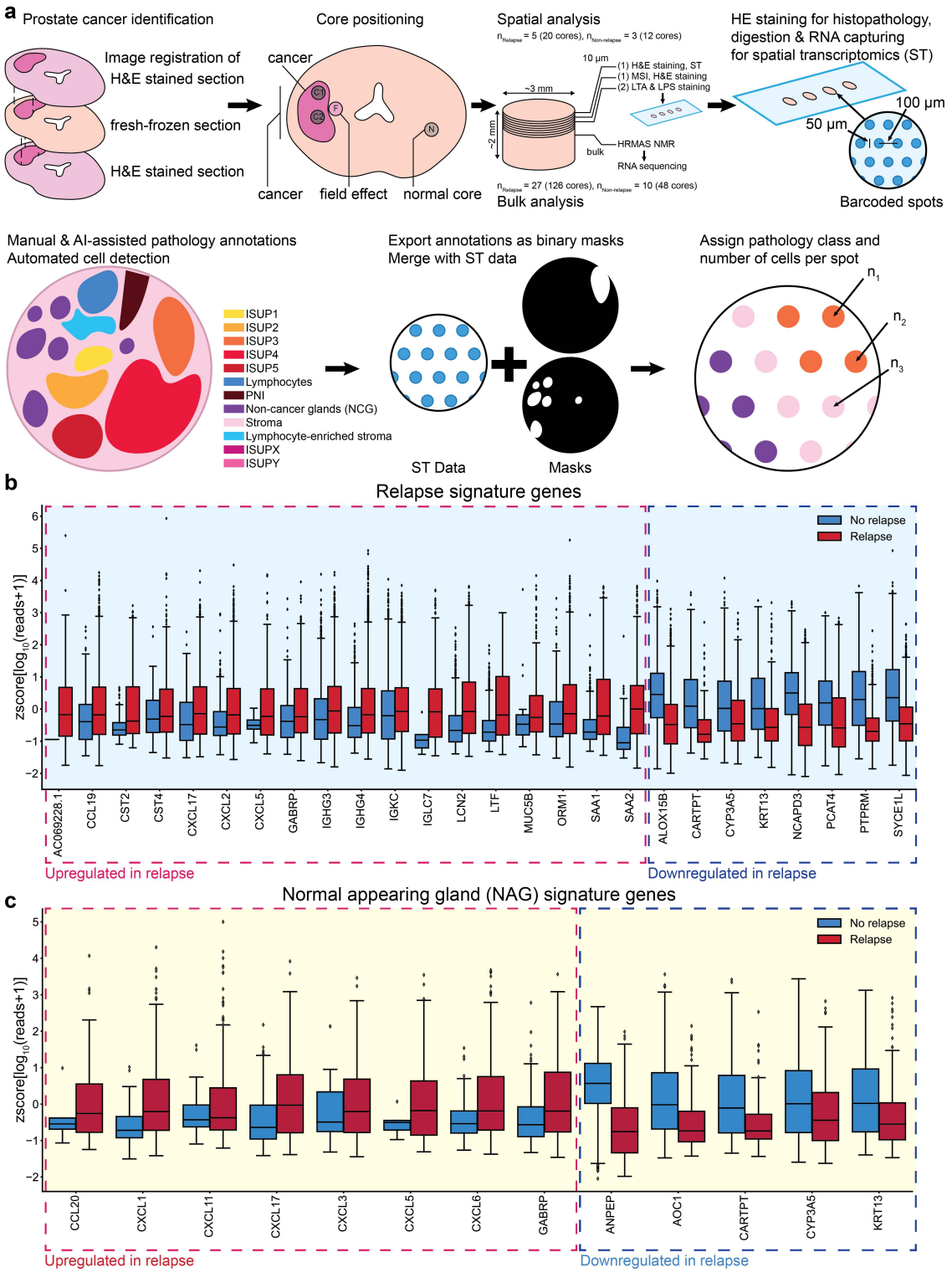

Figure 1 ***Multiomic spatial analysis of the prostate tumore microenvironment reveals gene signatures discriminating between relapsing and non-relapsing patients.*** *(a) Schematics of the collection of samples for bulk and spatial analysis of PCa tissue using bulk and spatial transcriptomics (ST) based on RNA sequencing, bulk metabolomics (high-resolution magic-angle spinning [HRMAS] NMR), spatial metabolomics (mass spectrometry imaging [MSI]), and histopathology staining (H&E, immunochemistry) using fresh frozen prostate tissue utilizing pathology annotations from adjacent FFPE sections to locate cancer and normal area. Subsequent cryo-section for spatial analysis, here exemplary shown for ST followed by spot classification according to per-section histopathology and cell count assessment. Expression of up- and downregulated genes*

forming the (b) Relapse gene signature (c) and normal appearing gland (NAG) signature over all spots with a count > 0 for the respective gene separated according to relapse status. The box and whisker plots are based on the z-score of the decadic logarithm of the normalized sequence reads.

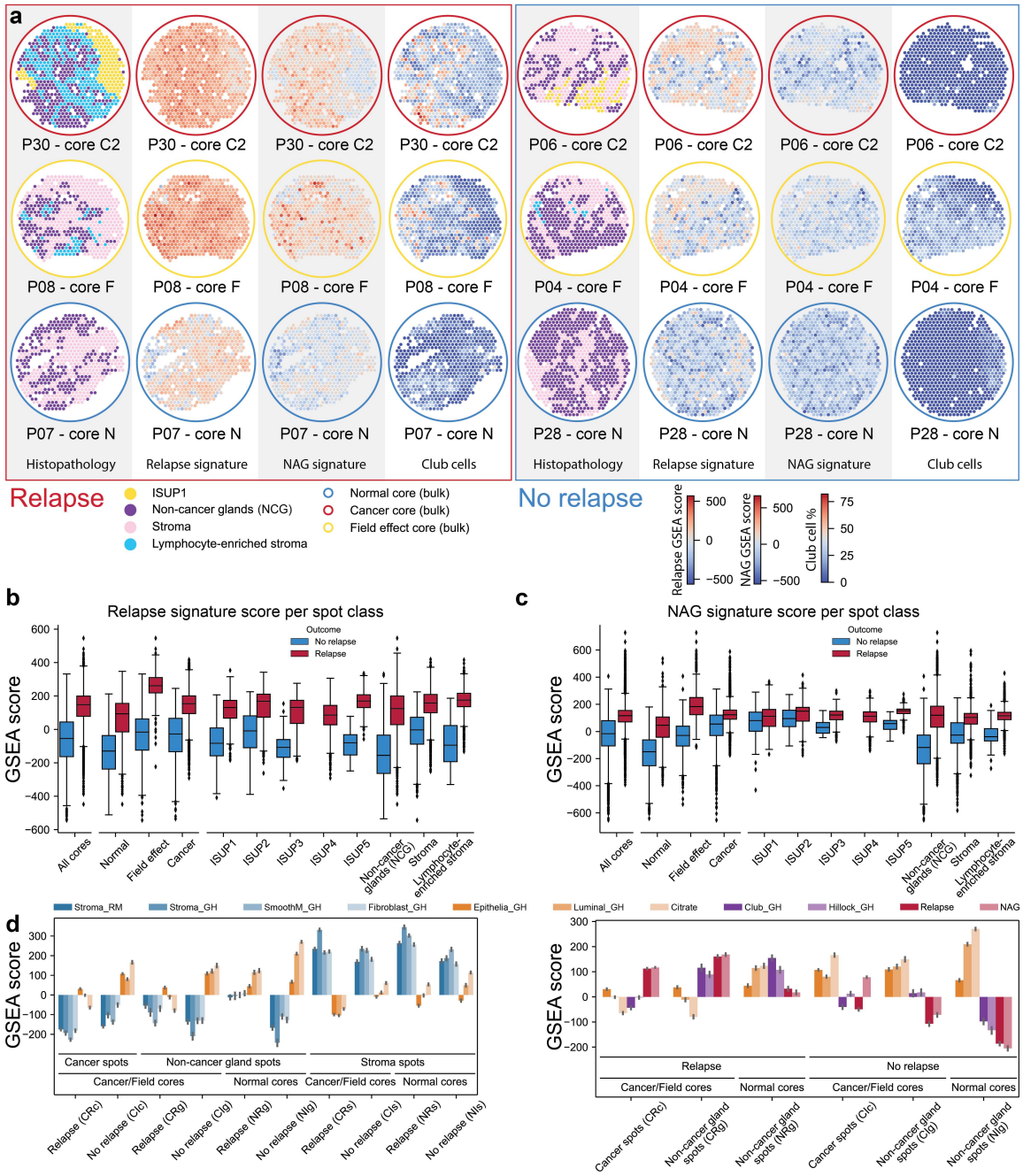

Figure 2 Relapse and NAG signature activity in prostate tissue. (a) Spatial distribution of Relapse and NAG signature activity, exemplary shown for one core type for each patient group, visualizes the global and uniform activity of the Relapse signature as compared to the NAG signature. Spots with high NAG signature activity appeared to also contain high estimated Club cell fractions. (b) Relapse signature activity was higher in all spot histology classes from relapsing patients (red) compared to non-relapse (blue), while (c) NAG signature activity was higher in non-cancer gland (NCG) spots and less pronounced also in stroma and cancer spots of relapsing patients and more prevalent in normal and field effect samples. (d) Mean scores of stromal activity gene sets (blue) in spots grouped by histopathology class (cancer, non-cancer gland, stroma), sample type (cancer & field, normal), and relapse status. Stromal activity was increased in stroma spots and decreased in NCG spots and vice-versa for selected epithelial gene sets (orange). (e) Mean activity of selected prostate epithelial gene sets, cell type specific gene set, Relapse, and NAG signature showed clear differences between relapse and non-relapsing patients. Both, NAG and

Relapse signature showed increased activity in relapsing patients accompanied by an increased activity of the Club signature and a slight reduction, especially in the NCG spots close to cancer, in luminal and citrate/spermine gene sets.

Relapse and NAG signature are associated with loss of luminal features and citrate secretion in glands

Considering that our gene signatures contained a high number of immune process related genes, we investigated which molecular processes and cell-types they were associated with. In addition to the Relapse and NAG signatures, we calculated for each spot *single sample Gene Set Enrichment Analysis* (ssGSEA, Markert et al.[13]) score using 38 gene sets characteristic for cell types and cellular phenotypes related to either normal prostate or PCa tissue, **Supplementary Figure 4 and Supplementary Table 2**). The *Relapse* ssGSEA score showed an overall predominant enrichment in spots from relapse patients compared to non-relapse patients (**Figure 2a and Supplementary Figure 3a**). This separation was clearly observed across all core types and histopathology classes **(Figure 2b and Supplementary Figure 3a)**. The distribution of the NAG signature ssGSEA score visualizes its capability to discriminate a sub-group of NCG spots. Although we observed an overall NAG signature enrichment in relapse compared to non-relapse patients, the spot histopathology class with the strongest separation were the NCG spots **(Figure 2c)**. Interestingly, not all NCG spots of relapse patients had a high NAG score, some even had negative scores (compare **Supplementary Figure 2a and 3b** NCG spots at 9 o'clock of section P30 – core N), and in case of high scores the surrounding stroma was often infiltrated by immune cells as can be seen in sections P08 – core F & N, P30 – core C2 (compare **Supplementary Figure 2a and 3b**).

Based on these observations we wanted to investigate if the NCG spots displaying high Relapse and NAG signature activity, despite the normal appearing histology, already underwent molecular aberrations. We suspected a dependency of the distance to cancer of such changes and thus defined 10 pseudo-bulk groups of ST spots based on the three major histology classes (Cancer, NCG, and Stroma), sample type cancer with field effect and normal) and patient relapse status (**Methods**) to simplify the analysis and still preserve to some degree the spatial nature of the data. Because of the low number of field effect cores, we decided to merge cancer and field effect unifying spots close to cancer and to obtain reasonable spot numbers in each of the 10 pseudo-bulk groups (863 to 4263 spots/group), as well as spots from all patients belonging to their respective subgroups to allow a reliable ssGSEA. We first validated our ssGSEA approach using gene sets for stroma and gland, the two most well-defined prostate tissue compartments [12]. All stroma spot groups showed strong enrichment for the four stroma related signatures (**Figure 2d**), and the gene signatures 'Epithelia_GH', 'Luminal_GH' and 'Citrate' (see **Supplementary Table 2** for details) were generally enriched in normal core NCG spot groups with higher scores in spots from non-relapse patients (**Figure 2d**), confirming the validity of our pseudo-bulk approach for ST data. Further, we observed that these gland signatures were depleted in NCG spots closer to cancer in relapse patients but not in non-relapsing patients. Interestingly, NAG and Relapse signatures followed an inverse trend, they were enriched in relapse patients where the gland signatures were depleted and vice-versa (**Figure 2e**). Additionally, we observed normal gland signature enrichment in cancer spots from non-relapse patients, but depletion in relapse patients. This finding supports our previous observations that prostate secretory genes are more depleted in tumors from relapse patients [14]. In conjunction, this hints at molecular changes in the NCG regions of relapse patients on the transcriptional level eventually resulting in the loss of luminal characteristics and citrate secretion capability of glands typical for PCa displaying high Relapse and/or NAG activity. This supports previous finds that the switch to a molecular cancer phenotype happens early in PCa before they are manifested in visible morphological changes in the tissue [7, 15, 16].

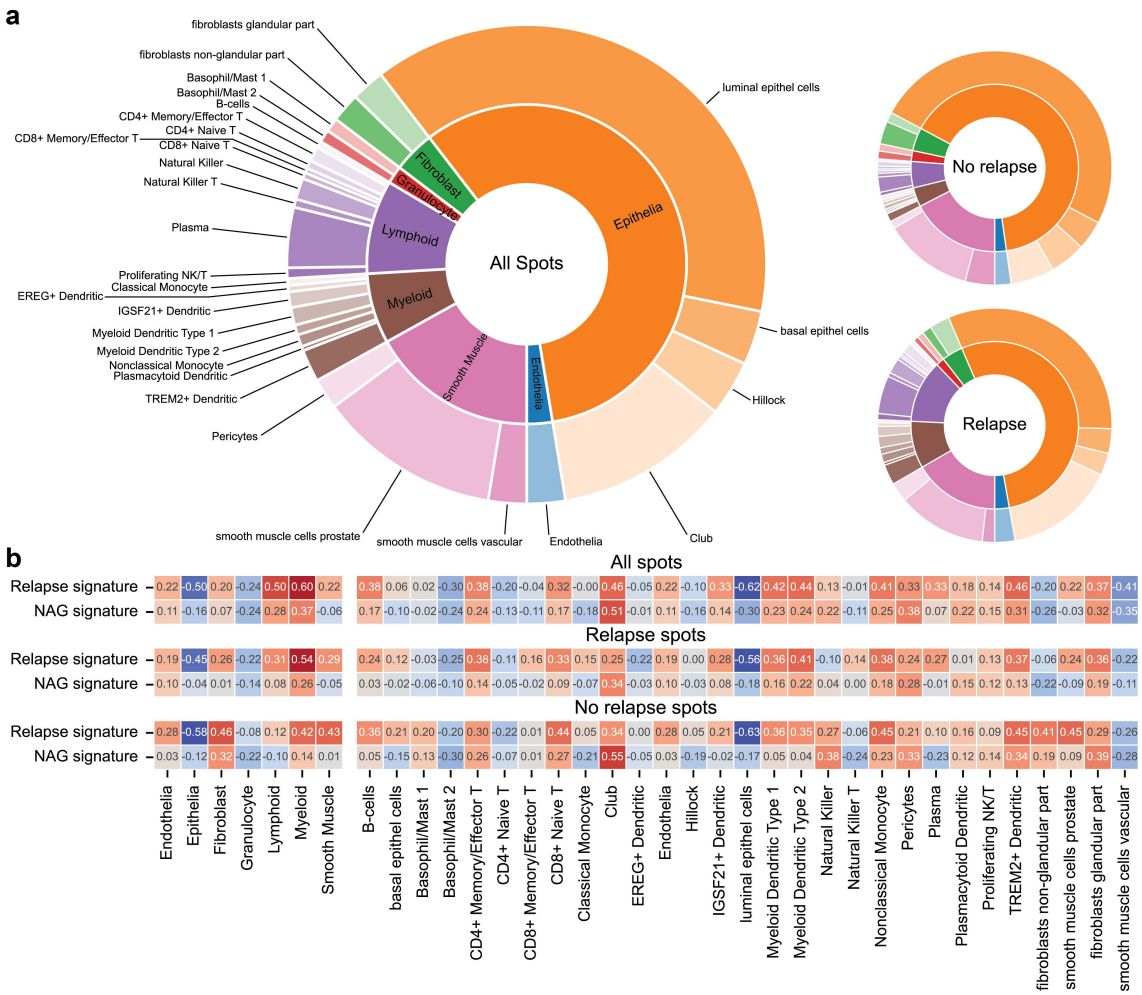

Figure 3 Cell-type composition of ST spots. Using cell-type specific RNA expression profiles derived from scRNAseq data we were able to deconvolute each ST spot into its cell-type composition. (a) The accumulated cell-type fractions are shown for all spots (left, large chart) and separated by relapse status (right, 2 smaller charts). (b) Spearman correlation coefficients calculated for cell-types and signature activity for all spots (top), spots from relapsing patients (middle) and spots from non-relapsing patients (bottom) visualized by color (red = positive, blue = negative correlation).

Relapse and NAG signature are associated with Club-like cell and immune cell enrichment

To understand potential associations of the Relapse and NAG signatures with specific cell populations present in the tissue of relapse patients, we first investigated which of the cell type specific gene sets of the 38 used in the pseudo-bulk approach were co-enriched in the same tissue regions with a focus on the NCG close to the cancer (Supplemental Figure S4b, CRg group). We saw an enrichment of immune cells from the lymphoid and myeloid lineages in this spot group (CRg) and even in the NCGs further away from the cancer (NRg) of relapse patients compared to respective groups (CIg & NIg) in non-relapsing patients (**Supplemental Figure S4b**). Of note, we also observed an enrichment of the gene sets for Club and Hillock cells in these spot groups from relapsing but not from non-relapsing patients (**Figure 2e and Supplemental Figure S4b**).

Motivated by the correlation of our signatures with these cell type specific signatures, we decided to further investigate signature and cell-type correlations on the individual spot level. Since ST data captures RNA from roughly 10-30 cells in each individual spot, the spot expression profiles originate

from a mixture of cell-types and is quite sparse. Thus, we choose to deconvolute each spot using *stereoscope*, a tool specifically developed to estimate cell-type compositions in ST spots by learning cell-type specific gene expression profiles from single-cell RNA-seq data [17] instead of continuing solely with the gene set enrichment approach. The stereoscope model was trained on publicly available single-cell RNA-seq data obtained from normal prostate tissue [9].

Using this approach, we found that the overall cell-type distribution was dominated by epithelial cells, followed by a large fraction of smooth muscle cells, a comparably large fraction of immune cells, and smaller fractions of fibroblasts and endothelial cells (**Figure 3a, b**). Interestingly, the most prominent difference between relapse and non-relapse spots was the relative increase of immune cells and Club-like cells (**Figure 3a**). The correlation of histopathology with cell-type composition showed that NCGs correlated positively with epithelial cell types and negatively with fibroblasts and smooth muscle cells while stroma inversely correlated with these cell-type **(Supplementary Figure 5)**. Further, luminal epithelial cells were only weakly positively correlated with ISUP1 and this correlation gradually decreased with increasing ISUP grade to reach a weak negative correlation with ISUP5, reflecting the loss of luminal characteristics in this tissue. In conjunction, these results confirm our observations using the ssGSEA, pseudo-bulk approach and thus validated the underlying stereoscope model.

To further narrow down cell type associations with the Relapse and NAG signatures we next calculated the spearman correlation of the signatures with the stereoscope-derived cell fractions. We found that immune cells of the lymphoid and myeloid lineages but not granulocytes were positively associated with the Relapse and NAG signatures, confirming the results from the pseudo-bulk approach on the individual spot level. Further, the earlier described loss of luminal cell-type characteristic along with Relapse signature activity was reflected in a strong negative correlation of the Relapse signature and a moderate negative correlation of the NAG signature with luminal epithelial cells. Both signatures were positively correlated with Club-like cells but interestingly no clear correlation with hillock cells was observed **(Figure 3b)**. The correlation with Club-like cells agrees with our observation from the ssGSEA pseudo-bulk analysis, while the even slightly negative correlation with the hillock cells appears to contradict the results above. The KRT13 gene is downregulated in both signature active regions (**Figure 1b**) and hillock cells are characterized as KRT13+ the here observed negative correlation appears plausible. Nevertheless, Hillock cells are not well described in the literature, especially in the human prostate, making it likely that both approaches (stereoscope and ssGSEA) might capture other closely related cell types leading to these indifferent results. Thus, we decided to disregard the Hillock cells and rather focus on the enrichment of Club-like cells specifically in the NCG spots close to the cancer of relapsing patients that coincided with a strong depletion of luminal and citrate secretion signatures. Overall, loss of luminal characteristics and lower citrate secretion in these NCGs indicates a switch from the molecular phenotype of the normal healthy prostate – closest resemblance in our data are the normal core NCGs from non-relapse patients – to the molecular phenotype of PCa. In conclusion, these "defunctionalizing" NCGs in relapse patients were enriched with Club-like and immune cells while simultaneously characterized by high Relapse signature and the more gland specific NAG signature activity.

Club and Hillock cells were initially characterized in the lung [18] and shortly after in benign prostate in a single-cell study [8]. In a normal healthy prostate, Club and Hillock cells locate in the urothelial and proximal prostate zone, which fit with studies in mice where they have a role in budding from the urothelia in early prostate development [19]. However, subsequent single-cell RNAseq and ST studies observed somewhat surprisingly Club and Hillock cell populations in the prostate peripheral zone in association with PCa [4, 5], which was also confirmed by the presence of Club cell protein markers in regions adjacent to prostate tumor tissue histologically associated with Proliferative Inflammatory

Atrophy (PIA) [20]. The enrichment of Club cells in combination with reduced Androgen Receptor (AR) signaling measure in clinical tissue specimens have previously been shown as an effect of treatment with 5ARI and androgen deprivation therapy [21-23].

Chemokines in Relapse and NAG signature likely to originate from Club-like cells

To gain further insight into the cellular origin of the individual genes of our signatures, we looked at the correlation of those genes with the cell type compositions obtained by gene expression deconvolution (see methods and **Supplementary Figure 6**). For the Relapse signature, the upregulated genes LCN2, LTF, SAA1, SAA2, CXCL17 were strongly (Spearman coefficient [sCC] >= 0.25) and the genes GABRP, IGHG3, IHGH4, IGLC7, MUC5B, CCL19, CXCL2, CXCL5 were weakly (sCC >= 0.15) positively correlated with Club cells (**Supplementary Figure 6 top**). Cells of myeloid lineage representing the first line of defense against infections were also positively correlated with these genes and further strongly (sCC >= 0.37) positively correlated with LTF, CCL19, and some of the immunoglobulins upregulated in the Relapse signature (IGHG3, IGKC, IGLC2). The same immunoglobulins in addition to IGHG4 were also strongly positively correlated with lymphoid cells. In contrast, luminal epithelial cells were positively correlated with the downregulated genes ALOX15B, ANPEP, CARTPT, CYP3A5, NCAPD3, PCAT4, and PTPRM (sCC >= 0.20). For the NAG signature genes (**Supplementary Figure 6 bottom**), we found that the additional chemokines CXCL1, 3, 6, 11, CCL20 were all also positively correlated (sCC >= 0.10) with Club cells and cells of the myeloid lineage. Of note, the expression of these genes, apart from CXCL11, was mostly negatively correlated with luminal epithelial cells and other cell types of the lymphoid or endothelial lineages. These findings strengthen the observed link between Club-like cells, an inflammatory immune response, our signatures, and aggressive PCa. Reduction of ALOX15B, PTPRM, and ANPEP have been reported as progressors of and were associated with high-grade PCa [14, 24-26]. Interestingly, NCAPD3 has supposedly tumor-promoting effects in PCa [27] while expression was also associated with reduced recurrence after radical prostatectomy [28], thus confirming our observation that a reduction was associated with more aggressive PCa. Further, CYP3A5 is known to be a modulator of AR signaling in PCa [29] while the role of CARTPT, a known oncogene, in PCa is not well understood [30]. LCN2, LTF, MUC5B, CXCL1, CXCL6, and CXCL17 are enriched in so called effector Club cells of the lung tissue playing a crucial role in the first line of immune response [31]. Our findings indicate that the observed enrichment of the chemokines CXCL1, 3, 5, 6, 11, 17, CCL20 is probably caused by a population of Club-like cells similar in function to lung effector Club cells in the respective NCGs causing the observed infiltration of immune cells amplifying the chemokine signaling. Except for CXCL17, all of these chemokines are pro-inflammatory and attract immune cells [32] and are implicated in pro- or anti-tumor immunity depending on the respective chemokine ligand-receptor interaction and immune cell type [33]. In conclusion, by investigating the individual genes both in the Relapse and the NAG signature, the observed gene correlations provide evidence of potential pro-inflammatory chemokine signaling from prostate effector Club cell-like cells and a potential role in aggressive PCa.

Chemokine receptor ACKR1 dominant receptor of CXC-chemokines of the NAG signature in relapse patients

Chemokines are typically detected via specific chemokine receptors resulting in chemotaxis of the target cells. After identifying Club-like cells as the most likely source for the chemokine secretion captured in the NAG signature, we wanted to investigate which chemokine receptors were detected in the ST data and what potential receptor-ligand interactions were active. Of all the chemokine receptors, we only detected expression of CXCR4 and ACKR1 in the ST data (Supplementary Figure 7a) of which only ACKR1 is known to respond to the CXC chemokines of the NAG signature. Bulk transcriptomics data obtained from 174 samples of 37 patients (including the 8 patients of the ST data

cohort) demonstrated that both CXCR4 and ACKR1 together with ACKR3 and CCR1 are amongst the highest expressed chemokine receptors in prostate tissue (Supplementary Figure 7b). Nevertheless, to investigate potential signaling across different tissue types of the chemokines of the NAG signature in relapse patients, we performed a cellphoneDB analysis of the ST data using the histopathology classes as groups and limiting the receptor-ligand interactions found in the OmniPathDB to those with at least one literature reference. To avoid a potential bias caused by data sparsity but also preserve some of the spatial information we choose to perform the analysis for all the relapse cores individually and combine the results but abstained from any further grouping using spot-to-spot distance or cell-type composition.

We found significant interaction of CXCL1, -3, -5, -6, and -11 with ACKR1 from NCGs to lymphocytes, stroma, and lymphocyte-enriched stroma spots (Figure 4a). Corresponding interactions were also observed from stroma and lymphocyte-enriched stroma to lymphocytes, stroma, and lymphocyte-enriched stroma spots. Interestingly, CXCL1, 3, and 6 – ACKR1 interactions were also present with NCG spots as origin and ISUP1 and NCG spots as receiver. Of note, we found a CXCL11-DPP4 interaction with NCG, stroma, and lymphocyte-enriched stroma as sender and NCG and cancer spots as receiver. The expression level of CXCL1, -3, -5, -6, -11, ACKR1, and DPP4 in spots from relapsing patients supports these interactions (Figure 4b). We found NCG and stroma spots to be the main source for these CXC chemokines while the for the cancer spots the expression was lower and mainly detected in the low-grade spots. ACKR1 was detected in all spot classes but was highest in both stroma classes and the lymphocyte spots. Compared to ACKR1, DPP4 showed a high expression in all spot classes except for lymphocyte spots. To gain insight into the cell types that express ACKR1 and DPP4, but also CXCR4, we looked at the correlation between their expression and the cell type composition for each ST spot (Figure 4c). ACKR1 was positively correlated with endothelial cells (sCC = 0.29) and slightly negatively correlated with luminal epithelial cells (sCC = -0.12). In contrast, DPP4 was negatively (sCC = -0.20) correlated with endothelial cells and strongly positively (sCC = 0.53) correlated with luminal epithelial cells. CXCR4 was positively correlated with cells of the myeloid (sCC = 0.37) and lymphoid (sCC = 0.28) linages and as ACKR1 also negatively correlated with luminal epithelial cells (sCC = -0.26).

ACKR1, also known as the Duffy antigen receptor, was initially discovered on erythrocytes and loss of expression is associated with malaria resistance [34]. Apart from erythrocytes, ACKR1 is expressed on endothelial cells of the lungs. Here ACKR1 is involved in propagation of CXC chemokine signaling in inflammatory processes, for example by translocating chemokines from the basal to the apical side resulting in the recruitment of circulating immune cells. Considering that our data suggests ACKR1 to be mainly expressed on endothelium in the prostate and the observed increased immune cell infiltration a similar role in the prostate as in the lungs appears plausible. Interestingly, ACKR1's role in cancer has been reported as dominantly protective against tumor metastasis, increased proliferation, and is associated with positive outcomes [35]. Nevertheless, in PCa reduced ACRK1 expression on erythrocytes in men of African descent appeared not to be linked to aggressiveness [36, 37] while ACKR1-deficient mice showed increased tumor growth [38]. In contrast, ACKR3 expression together with CXCR4 is associated with cancer promoting effects [39]. Even though, of those we only detected CXCR4 in the ST data, we found ACKR3 to be equally high expressed as ACKR1 in our bulk transcriptomics data. DPP4 is known to cleave chemokines at the N-terminus resulting and altered signaling and diverse effects on inflammatory processes [40]. Considering that we found ANPEP, another known modulator of CXCL11 signaling [41], to be downregulated in relapse patients puts the proposed CXCL11-DDP4 interaction into an interesting perspective strongly suggesting further studies on the role of peptidase-based alteration of chemokine signaling in PCa.

In conclusion, we found indications that CXCL-ACKR1 signaling might be a dominant chemokine-chemokine receptor interaction in the microenvironment in and around the NAG signature positive regions. Further, this signaling could possibly be modulated through DPP4 and ANPEP.

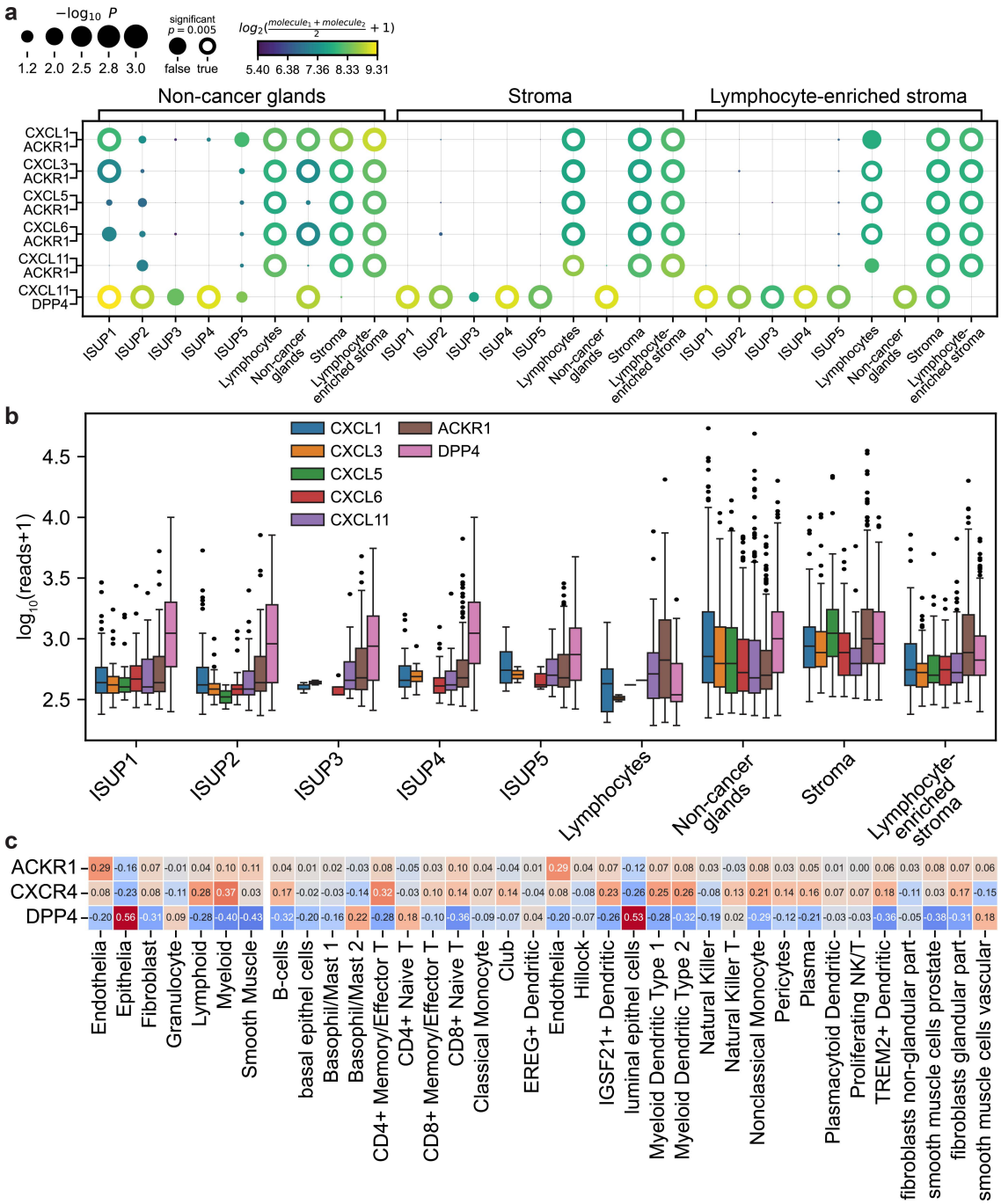

Figure 4 Chemokine receptor-ligand interaction in tissue from relapse patients. (a) Potential receptor-ligand interactions of the CXC chemokines of the NAG signature with ACKR1 and DPP4 between different tissue types found by combining the CellPhoneDB results obtained from ST data of each of the cores from relapsing patients. The means of the average expression of the receptor-ligand pair are visualized with a color gradient and the p-values by the size of the circles. Receptor-ligand pairs are shown on the y-axis and interacting spot class pairs are given on the top and bottom x-axis. (b) Expression of the CXC chemokines of the NAG signature, the chemokine receptor ACKR1 and DPP4 in tissue from relapse patients. Shown are only data from spots with reads > 0 as box-and-whisker plots. (c) Correlation of ACKR1, CXCR4, and DPP4 expression with cell type fractions per spot. Shown are the spearman correlation coefficients as numbers and additionally visualized by color (blue

= negative, red = positive correlation). Corresponding correlations for the CXC-chemokines are visualized in Supplemental Fig. 6.

No obvious correlation of bacterial infections and NAG signature

Acute and chronic bacterial prostatitis are common [42] and thus a likely cause for the observed inflammation. Despite this, we could not detect expression of cytokines typically induced by bacteria during acute infection, such as IL-6 and TNF-α in the ST data. We further investigated this by staining serial sections for lipopolysaccharides (LPS) and lipoteichoic acid (LTA) to detect gram-negative and gram-positive bacteria in the adjacent tissue. Following affine co-registration of the corresponding serial sections we calculated an interpolated NAG signature activity density map for each of these stained sections. Next, we ran an automated cell detection and assigned an estimated signature activity and staining intensity to each cell (**Supplementary Figure 8**).Only a small fraction of the cells stained positive for LTA or LPS (359 of 718901, 374 of 746976 cells analyzed in total) and we did not find a clear positive correlation between Relapse or NAG signature activity and LTA or LPS staining. In conclusion, we did not detect any signs of an acute bacterial prostatitis as cause for the observed inflammatory response in these regions of the tissue. Regarding chronic bacterial prostatitis as a contributing factor, the results remain inconclusive. The detected low-level presence of LPS and LTA in regions with NAG signature activity might suggest some bacterial contribution possibly at an earlier time-point.

Relapse and NAG signature associated with altered metabolism

To reveal the metabolomic phenotypes of the Relapse and the NAG signature, we investigated spatial metabolomics data obtained by MALDI MSI on serial sections adjacent to sections that were used to obtain ST data (**Figure 1a**). We were interested if the reduced expression of genes associated with luminal characteristics and citrate secretion we observed in regions with NAG and Relapse signature activity resulted in corresponding metabolic changes in these regions. MSI data were registered to the corresponding ST data and median relative levels of putatively identified metabolites for each ST spot were calculated (unpublished method yet). By grouping the ST spots according to the ssGSEA score of the Relapse and the NAG signature into spots with significant high, low, or not significantly changed score, we found that citrate, zinc, and ATP were reduced in both Relapse and NAG signature active regions **(Figure 5**). Furthermore, we detected an increase of AMP, ADP, glutathione, glucose, glutamate, glutamine, *N*-acetylaspartate (NAA), urate, and taurine in those spots. Roughly half of the high Relapse signature activity group were stroma spots (56%) while the other half were approximately equal amounts of cancer (10% high grade and 8% low grade) and NCG (22%) spots. Lymphocyte spots made up roughly 3% of the Relapse signature active region (**Figure 5b**). In contrast, NAG high regions were dominated by NCG (55%) spots with a clearly lower high grade (3%) and slightly higher low grade (15%) fraction. Lymphocyte spots were only a very small percentage (0.6%, **Figure 5c**).

These findings show that high activity of both signatures is associated with metabolic changes in the respective regions. The histopathological composition of the Relapse signature high region with its approximate 2:1:1 stroma:cancer:NCG ratio reflects the average composition of the ST sections (**Supplementary Figure 2a**) and in general roughly that of PCa tissue [43]. Consistently, the metabolic phenotype observed in these regions displayed the typical hallmarks of PCa metabolism: Reduced citrate and zinc, indicators for an increased glycolysis, and signs for an increased glutamine consumption [44]. Interestingly, the high NAG signature regions, even though mainly containing NCG spots, showed a very similar, cancer-like, metabolic phenotype (**Figure 5**). The reduction of zinc, typically understood to block aconitase to allow healthy prostate glands to maintain their physiologically high levels of citrate [45], in combination with the observed reduction of citrate, is a

clear indicator for loss of prostate characteristic luminal functions in NCG regions with high NAG signature activity. This agrees with our ST-based findings of reduced transcriptional activity of citrate secretion associated genes in the same regions. This implied change of the metabolic behavior of NCG adjacent to cancer areas has, to our knowledge, not been previously observed in PCa. The loss of gene expression associated with citrate secretion in NCGs from relapse cancer samples (**Figure 2e**) appears to be the most profound change of the prostate specific luminal cell-type characteristics. When inspecting the genes present in the Relapse signature, we found that two of the downregulated Relapse genes (*ALOX15B* and *NCAPD3*) were also central genes in our previously published network of genes for citrate secretion (Rye-2022-iScience), further strengthening the link between aggressive tumors and loss of citrate secretion in corresponding cancer adjacent NCGs. The observed increased glucose levels and build-up of AMP and reduction of ATP, accompanied by a potential shift to utilization of glutamate as an energy source suggested by the pronounced increase of NAA, glutamate, and glutamine indicate a high catabolic state in these regions. These metabolic changes show striking similarities to those typically observed in cancer or inflammation [46, 47]. The increased urate levels in these regions, indicative of a potential increased activity of the uric acid cycle, might be a further indicator for a high catabolic state. Interestingly, urate, and urate crystals, have been implicated in being a cause for prostatitis [48-50] and a factor leading to inflammation eventually contribution to prostate carcinogenesis [51]. The increase of taurine in these areas is interesting as it has been described as pro-apoptotic, anti-prolific, and anti-migratory [52] but also to mitigate the resulting oxidative stress from inflammation, typically increased in high catabolic tissue [53, 54].

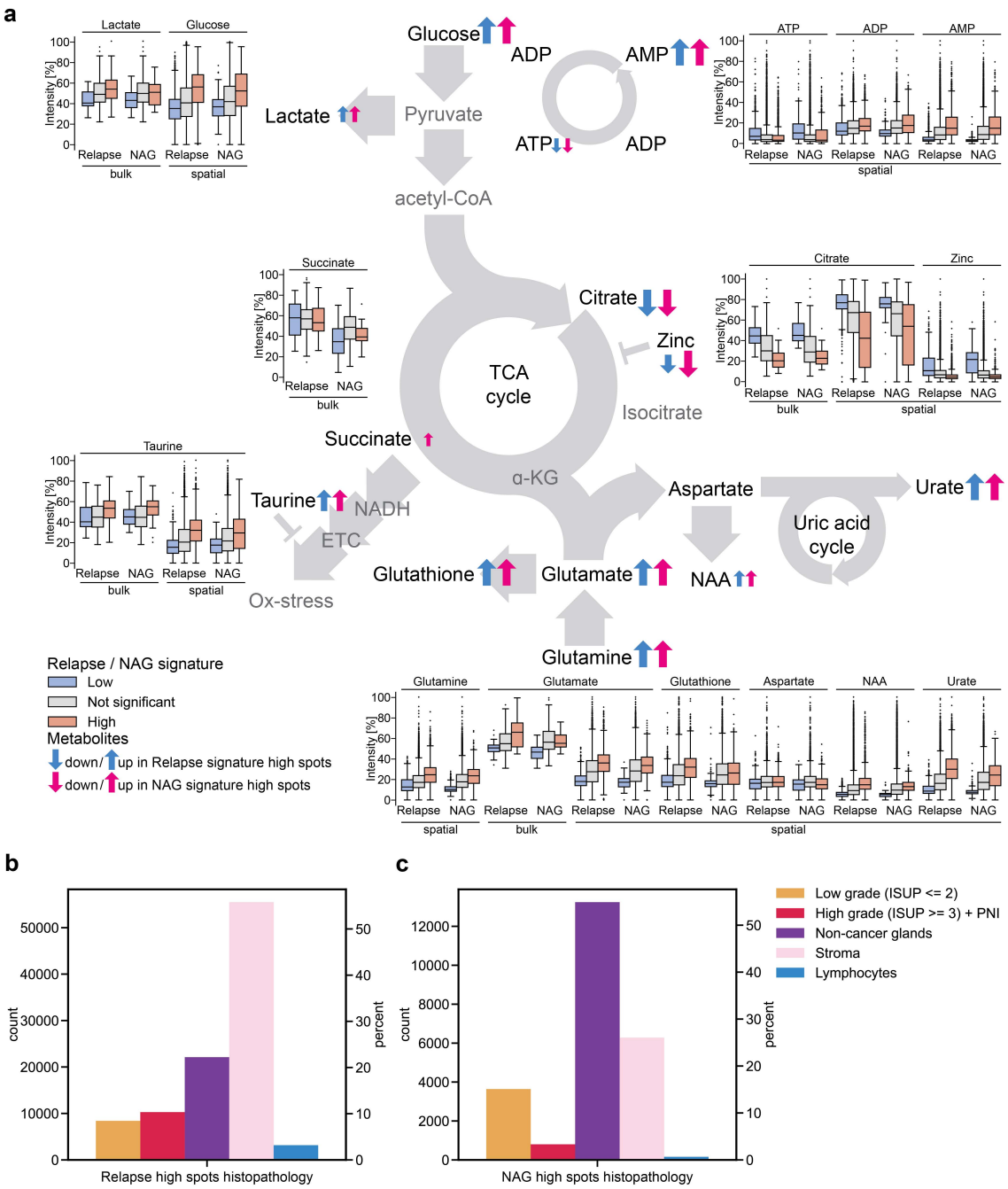

Figure 5 Changes of metabolite levels in relation to Relapse and NAG signature activity. (a) Shown are the relative intensities in % grouped by signature activity of metabolites detected either by MSI ("spatial") or HRMAS NMR ("bulk") placed according to their position in the indicated simplified metabolic pathways (glycolysis, TCA cycle, uric acid cycle). Metabolite level changes (up or down) in spots (spatial) or samples (bulk) with an increased signature activity compared to low signature activity are indicated with up or down arrows (blue = Relapse, magenta = NAG signature). Histopathology class composition of spots with (b) high Relapse and (c) NAG signature activities are shown as spot counts and percentage of all spots with high signature activity.

Relapse and NAG signature activity increased in bulk samples from relapse patients

The highly detailed, spatially resolved data from 8 patients allowed us to find both signatures and characterize associated biological processes. Unfortunately, in day-to-day clinical practice such data is rarely available and such detailed analysis hardly feasible. However, prostate biopsies are typically

collected and easier available for bulk molecular diagnostics. Thus, we wanted to elucidate if the Relapse signature and the NAG signature were detectable, predictive of relapse, and linked to the same metabolic changes in bulk samples of a larger patient cohort. We collected RNAseq data of 174 (no relapse n=48, relapse n=126) samples (classified as either cancer, field effect, or normal) from 37 (no relapse n=10, relapse n=27) patients after we measured the metabolic composition using HRMAS NMR (**Figure 5, Supplementary Figure 9 & 10**). The ssGSEA scores for the Relapse signature were higher in samples from relapsing patients (**Supplementary Figure 9a**). The strongest signal originated from cancer samples while the difference in normal and field effect samples was less prominent. Nevertheless, receiver operating characteristics (ROC) resulted in an area under the curve (AUC) of 0.75 (**Supplementary Figure 9b**). A per patient analysis revealed strong patient to patient variations with at least one clear outlier in the non-relapsing group (P05, **Supplementary Figure 9c**). Further, for the NAG signature we detected a weaker difference in activity between relapse and no relapse patients as compared to the Relapse signature with an AUC of 0.66 of the ROC (**Supplementary Figure 10**). Both groups had cores with high and low signature activity to the point that on average the signature activity was even slightly higher in normal and field effect cores of non-relapsing patients. A closer look at the per patient signature activity distribution (**Supplementary Figure 10c**) revealed that this effect was mainly caused by patient-to-patient variability. For example, non-relapsing patients P05 and P32 had cores with high signature activity while relapsing patients P09 and P25 had low signature activity. Interestingly, the overall difference – the variation around the mean activity – was also much smaller in bulk data as compared to ST data. From this we conclude, that both signatures derived from ST data are still measurable but only the Relapse signature still holds predictive power in bulk data. Using ST data, we detected Relapse signature activity in all parts of the tissue, including stroma and high-grade cancer, while the NAG signature was mainly active in some of the NCG regions in the TME. Thus, it appears reasonable that the predictive power of the Relapse signature is, to some extent, independent of the spatial information while the NAG signature requires precisely linked tissue morphology to unfold its full potential. This clearly highlights the value of methods, like ST, with high-plexity and high spatial resolution to investigate otherwise hidden changes in the TME but also makes it clear that further studies utilizing such technologies are required to fully explore the link between PCa relapse and these aberrant NCG regions.

Next, we analyzed the obtained metabolite data from these samples by grouping, correspondingly to the spatially resolved data, by significantly high, low or not significantly changed signature activity (**Figure 5**). We observed a reduction of citrate in samples with both high Relapse and NAG signature activity. Further, lactate, glutamate, taurine, and succinate were increased in these samples. These findings show a comparable metabolic phenotype linked to increased signature activity as we found in and discussed for the spatially resolved data. Both signatures are associated with loss of normal prostate glandular function indicated by a reduction of citrate and indicators for an increased catabolism. As discussed in the previous section about bulk RNAseq, bulk results in the context of the very localized NAG active NCG must be interpreted carefully. Nevertheless, the results from bulk metabolite analysis are in support of the spatially resolved data obtained using MSI for both signatures and in agreement with previous work as we discussed in the spatial metabolism section. Of note, the increase of lactate, a metabolite we could only detect using bulk HRMAS NMR, in samples with high NAG activity might suggest that the increased glycolysis in NAG active NCG regions could lead to accumulation of lactate. High intracellular levels of lactate have recently been reported to result in chromatin remoddeling and response to anti-androgen treatment in prostate organoids [55]

In conclusion, we could validate that the ST results from 8 patients translate to bulk data from a larger group of patients. Both, Relapse and NAG, signatures were detectable and on average more active in

bulk samples from relapse patients. Further, they were correlated to the same metabolic changes as observed with MSI supporting the findings from spatially resolved methods.

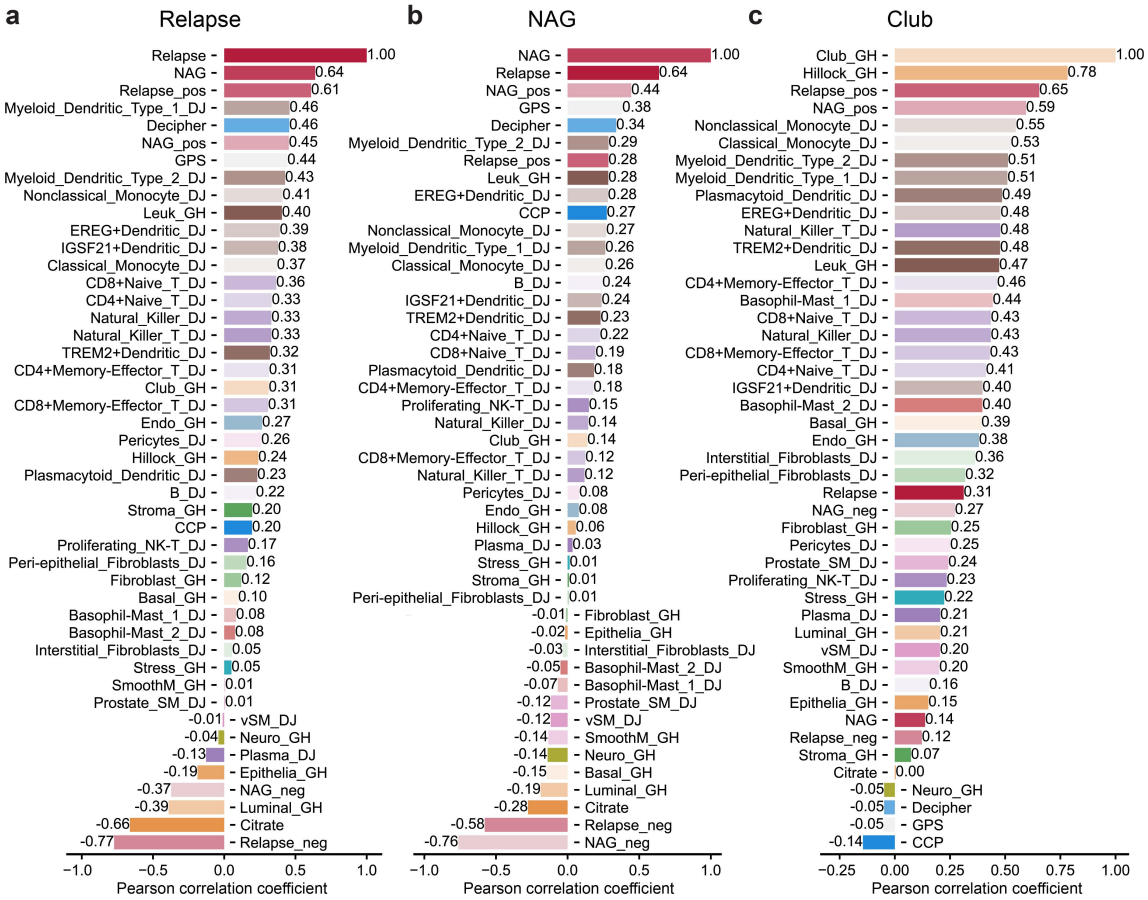

Figure 6 Average Pearson correlation between gene sets across 12 public data sets for a) Relapse signature, b) Normal appearing gland (NAG) and c) Club cell signature. Correlations are displayed for Relapse and NAG signature with positive (upregulated genes) and negative (downregulated genes) counterparts (shades of dark red) , epithelial linage gene sets, like Club, Luminal cells, and Citrate gene sets (shades of orange), immune cell gene sets (lymphoid – shades of purple, myeloid – shades of brown, granulocyte – shades of red), and genes from signatures known to be associated with aggressive PCa (GPS, Decipher and CCP, shades of blue). Correlations for all gene sets and individual public data sets are shown in Supplementary File 2 – Public Data.

Analysis in public bulk data supports association of Relapse and NAG signature with Club-like cells and reduced luminal function

To investigate whether our results could be traced in an even larger number of samples, specifically the association of our signatures with Club-like cells, citrate secretion, and luminal function observed in the ST data, we analyzed bulk gene expression data from publicly available cohorts (**Supplementary Table 3**). We calculated Pearson correlations between ssGSEA scores of Relapse, NAG, and Club gene set-based signatures with scores for the gene sets used previously in the ST data (**Supplementary Figure 4**) using 12 public datasets with a total of 2512 tissue samples from prostate and PCa. To estimate the correlation of our signatures with aggressive PCa, we also included gene sets based on three commercially used gene expression signatures (CCP, Decipher, GPS) for aggressive PCa in this analysis. Correlation analysis in public data in general confirmed the associations observed in ST data (**Figure 6, Supplementary File S2**)

The Relapse signature correlated with genes from GPS and Decipher, which supports the association between the Relapse signature and aggressive, recurrent cancer. The correlation was less strong for the CCP genes. The NAG signature also showed similar correlation preferences; however, the correlation values were weaker than for the Relapse signature. Both signatures also showed positive correlations to immune cells, but also here the correlation values were weaker for the NAG signature. Both signatures correlated negatively with the Citrate signature. Interestingly, the negative correlation to the Citrate signature was stronger compared to the negative correlation of Luminal cells, highlighting the relation of both our signatures with the secretory function of the luminal cells.

The Relapse and NAG signatures showed only intermediate (Relapse) or weak (NAG) positive correlation to Club-like cells in the public datasets. However, when we separated both signatures into their positive and negative contributions (up- and down-regulated genes respectively), we observed strong correlation with Club-like cells for the positive parts of both signatures (**Figure 6c**). This confirms that the observed associations between the two signatures with Club-like cells are extendable to larger patient cohorts. Interestingly, though inversely correlated in the ST data, the positive and negative counterparts of the NAG-signatures were not inversely correlated in the bulk data (**see Supplementary File 2**). We even observed a slight positive correlation between the positive and negative parts of the NAG signature. This could indicate that we are able to observe local compartmentalized signature combinations in ST data that is not detectable in bulk data.

Using public data, we could support the associations we found between our signatures and Club-like cells and reduced luminal functions, specifically citrate secretion. Further, we found supporting evidence that bulk transcriptomics data is limited compared to ST data in analyzing very localized gene expression-gen set associations. This indicates that local spatial transcriptome variations can help to drive recurrent cancer phenotypes not observable or detectable in bulk data. The different gene signature patterns in **(Figure 2e)** also supports this conclusion, where we see that it is certain combinations of gene set scores that characterizes the phenotypes in the different compartments – combinations which are probably too confounded to be detected in bulk data.

Conclusion

In this study we found two novel gene expression signatures capturing changes in the TME of PCa. We uncovered a strong link between Club-like cells, our signatures, and transcriptional and metabolic changes, specifically changes of citrate secretion in NCGs of patients with aggressive PCa. Further, we found indications that chemokines, major components in our signatures, are released by Club-like cells and are potentially responsible for the increased immune cell infiltration in and around these regions. In conjunction with the loss of citrate levels and a metabolism shifted towards higher energy consumption, these findings suggest a critical role of chemokines in the development and progression of PCa by modulating the TME and influencing various cellular processes. The increased expression of chemokines in PCa tissues highlights their potential as diagnostic and prognostic markers. Moreover, targeting chemokines and their receptors represents an attractive therapeutic strategy for combating PCa. Further research is warranted to unravel the intricate mechanisms underlying chemokine-mediated tumor progression, their role in altering prostate metabolism, and to explore their therapeutic potential fully.

Methods

Patient inclusion and sample collection

The study utilized human prostate tissue samples obtained from PCa patients who gave informed written consent before undergoing radical prostatectomy at St. Olav's Hospital in Trondheim between

2008 and 2016. None of the patients had received any treatment prior to their surgery (further clinical details listed in Supplementary Table 1). This research received approval from the regional ethical committee of Central Norway (identifier 2017/576) and adhered to both national and EU ethical regulations.

In total, tissue samples from 37 patients were included in this study. Among them, ten patients remained relapse-free for >10 years following surgery, while twenty-seven patients experienced relapse (biochemical recurrence (PSA > 0.1 ng/ml) and/or confirmed metastasis). We collected 174 samples (no relapse n=48, relapse n=126) from all these 37 patients (no relapse n=10, relapse n=27). Of these samples, we selected for spatially resolved methods 32 samples (no relapse n=12, relapse n=20) from 8 of the 37 patients (no relapse n=3, relapse n=5) choosing relapse patients with confirmed metastasis within three years. All samples were obtained by taking a 2 mm thick slice from the middle of the prostate (transverse plane) immediately after surgical removal. This slice was snap frozen and stored at -80 °C following the procedure described by Bertilsson et al. [56]. The collection of tissue slices and their storage were conducted by skilled personnel at Biobank1® (St. Olav's University Hospital in Trondheim). From each prostate slice we collected 8 to 13 tissue cores (3 mm in diameter) by using our in-house developed drilling device based on a previously described method [56]. For spatially resolved methods, we selected four samples per patient based on histopathology evaluation of hematoxylin erythrosine saffron (HES) stained tissue sections of each drilled sample. If applicable, we acquired two samples with cancerous tissue, one sample with non-cancerous morphology close to the cancerous region, and one sample with non-cancerous morphology distant from the cancerous area for each patient.

Tissue serial sectioning

For all tissue samples we collected several 10 µm-thick sections through serial cryosectioning at -20°C using a Cryostar NX70 (Thermo Fisher). The tissue sections destined for spatial transcriptomics analysis were placed on Visium slides according to manufacturer's recommendations. Remaining tissue sections were collected for other methodologies (many of which not presented in this study) and were placed on other types of slides such as super frost, conductive slides and membrane slides. Sections destined for matrix-assisted laser desorption ionization (MALDI) mass spectrometry imaging (MSI) were placed on conductive IntelliSlides (Bruker Daltonics) and vacuum-packed as described by Andersen et al. [57]. All sections were kept cold during sectioning (-20°C) and stored at -80°C until further use. Material remaining after sectioning was stored at -80°C until use for bulk metabolomics (HRMAS NMR) and transcriptomics (RNAseq).

RNA isolation, cDNA library generation and sequencing

For spatial transcriptomics profiling we used the Visium Spatial Gene Expression Slide & Reagent kit (10X Genomics) following the manufacturers manual. Shortly before RNA extraction, tissue sections were fixated with 100% methanol, stained with hematoxylin and eosin (H&E) and digitally scanned at 20x magnification (Olympus VS120-S5). To ensure proper optical focus, a coverslip was temporarily placed on the tissue section and then gently removed after scanning. RNA was extracted by exposing the tissue sections to a permeabilization agent for 12 minutes. Optimal extraction time was previously determined with the Visium Spatial Tissue Optimization Slide & Reagent kit (10X Genomics). A second strand mix was added to create a complementary strand, and subsequently, cDNA was amplified using real-time qPCR. The amplified cDNA library was quantified using the QuantStudio™ 5 Real-Time PCR System (Thermo Fisher) through qPCR, and the cDNA libraries were stored at -20°C until further use. Paired-end sequencing was conducted using the Illumina NextSeq 500 instrument (Illumina®, San Diego, USA) and the NextSeq 500/550 High Output kit v2.5 (150 cycles). Bulk RNAseq samples used in this study was performed as previously described [58].

Generation of raw count tables

ST sample data were processed using 10x genomics space ranger software package (version 1.0.0) according to manufacturer's recommendations. BCL files were demultiplexed to FASTQ files using spaceranger mkfastq. Raw count tables were generated from these FASTQ files together with the H&E stained images and the human reference transcriptome GRCh38 version 3.0.0 per sample using spaceranger count. For the bulk samples, raw base call (BCL) files generated by Illumina sequencer were processed as previously described [58].

Cell detection and number of cells per ST spot calculation

For each sample, cells were detected using the build-in-cell-detection feature of QuPath (version 0.2.3)[59] utilizing H&E staining segmentation of nuclei to generate a list of nuclei centroids. For each spot, the number of centroids inside the spot area were counted to obtain the cells per spot count values. Data export from QuPath, merging with spatial transcriptomics spots, and cell counting were done using in-house developed groovy and python scripts and a python package is available on github [https://github.com/sekro/qupath_scripts, https://github.com/sekro/spatial_transcriptomics_toolbox]

Histopathology

Two experienced uropathologists (T.V. and Ø.S.) independently evaluated the H&E-stained sections from all 32 spatial transcriptomics samples in QuPath (version 0.2.3). They annotated cancer areas according to the International Society for Urological Pathology (ISUP) Grade Group (GG) system[60] and aggregates of lymphocytes. Glands of uncertain cancer status were also annotated. We aimed to assign pure Gleason patterns to distinct cancer glands where possible. For example, well-defined separate areas of Gleason pattern 3 and 4 were annotated as IUSP GG 1 and 4, respectively, instead of one area of ISUP GG 2 or 3 (Gleason 3+4 or 4+3). For the downstream data analysis, a consensus pathology annotation was reached in agreement with both pathologists. Gleason scores were transformed into ISUP GGs and labeled with ISUP1-5 accordingly. Cancer areas with uncertain grading were annotated as ISUPX (indecisive between ISUP3 and ISUP5) and ISUPY (indecisive between ISUP1 and ISUP4). Other section annotations included tissue borders, lumen, glands, stroma, and stroma with higher levels of lymphocytes (referred to as 'lymphocyte-enriched stroma').

Integration of Histopathology with Spatial Transcriptomics data

Digital histopathology annotations including annotations for tissue bounds, luminal spaces, tissue folds, and uncertain areas were exported as binary images from QuPath using an in-house developed groovy script [https://github.com/sekro/qupath_scripts/blob/main/export_for_st_toolbox.groovy]. Histopathology data were merged with spatial transcriptomics data using an in-house developed python package [https://github.com/sekro/spatial_transcriptomics_toolbox]. For each spot, the intersection with the binary maps for each annotation class were calculated as a percentage per ST spot. The area of each of these intersections was divided by the tissue containing area of the spatial transcriptomics spot. The resulting percentage values per annotation class per ST spot were accumulated in a table and used to assign each spot a histopathology class. First, spots were excluded if they contained less than 50% tissue, more than 50% folded or low staining quality tissue, or more than 80% luminal space. If a spot contained more than 55% stroma it was assigned the stroma or lymphocyte-enriched stroma class using the one with the higher value. Otherwise, the spot was assigned one of the ISUP-grades, perineural invasion (PNI), or lymphocyte classes if the respective area of one of these classes was above 50%. In a last step, spots that were not assigned stroma or any of the ISUP-grades, PNI, or lymphocyte classes and contained at least 30% non-cancer glands (NCG), were

assigned the class NCG. Spots not fulfilling any of the mentioned criteria were excluded from the analysis.

Spatial Transcriptomics data curation and normalization by number of cells per spot

Raw counts were normalized by dividing the counts by the number of cells for each spot (**Figure 1a, Supplementary Figure 1**). Normalized total counts per spot were calculated as the sum of all normalized counts and normalized number of detected genes per spot were obtained by counting genes with normalized counts > 0 for each spot. Spots with less than 100 normalized total counts or less than 40 normalized number of detected genes per spot were excluded.

Genes were only included if total raw count per gene over all spots was not zero and at least 10 counts for at least 10 spots were observed.

Deconvolution of spatial transcriptomics data

Each spot of the spatial transcriptomics data was deconvolved into estimated cell type fractions using stereoscope [17]. For single cell reference data we used publicly available human prostate single cell RNAseq data [9]. From this single cell data we obtained a list of 4324 highly variable genes using scanpy's implementation of the Seurat method [61, 62]. Stereoscope was run with this list of highly variable genes and the following parameters: sc epochs = 75000, sc batch size = 100, st epochs = 75000, st batch size = 100, learning rate = 0.01.

Identification of Relapse and Normal Appearing Gland (NAG) signatures

The ST spots were grouped according to the histopathology classes and analyzed for differences between relapsing and non-relapsing patients utilizing spatial information (see also **Supplementary Figure 2b**). ST data raw reads per cell values were decadic logarithm transformed prior scaling by 10000 to obtain human readable values ($reads_{log10} = log_{10}(reads_{\frac{raw}{n_{cells}}} * 10000 + 1)$) and used for all downstream analysis described in this section. To capture the variable genes in the ST data, we used two approaches: 1. We calculated for each histopathology class the relative standard deviation (RSD, standard deviation / sample mean) for each gene and saved the 5 genes with the highest RSD per class into a preliminary gene list. 2. To find genes that are variable compared to genes of similar average expression, we used the approach suggested by Satija et al. and calculated for each class the dispersion (mean/variance) for each gene [62]. Then, genes were binned according to their mean into 20 bins. Subsequently, dispersions were standardized by its respective genes bin mean and standard deviation to obtain bin-wise "expression-level normalized" z-scores for each dispersion. We added the 5 genes with the highest z-score dispersion per class to the preliminary gene list. Next, we added deregulated genes in relapsing patients per class to the preliminary gene list. Deregulated genes were defined as genes with an absolute difference of the means of the normalized expression of relapsing and non-relapsing patients larger than 1 (corresponding to a 10-fold change in expression) and a maximum RSD of 20% in the non-relapsing patient group.

The preliminary gene list was filtered by removing genes with 75% or more observations coming from only one sample or patient and that have been observed in 2.5% or less of all spots. Further, to rank the remaining genes according to their strength to differentiate between relapse and no relapse we calculated the min-max normalized zero-count-free median difference (ZFCMD) and the min-max normalized non-zero-reads spot count difference (NZRSCD), with

$$ZFCMD_g = \left|median\left(c_{Relapse,g}\right) - median\left(c_{Non-relapse,g}\right)\right|, for\ c > 0, with\ c = normalized\ counts\ for\ gene\ g$$

$NZRSCD_g = \frac{|n(S_{Relapse,g,c>0}) - n(S_{Non-relapse,g,c>0})|}{(n(S_{Relapse,g,c>0}) + n(S_{Non-relapse,g,c>0}))}$, with S = spots, g = gene, c = normalized counts for gene g. By excluding spots with 0 reads the ZFCMD can better capture intensity differences in the sparse ST data but gets more sensitive to outliers in cases of low number of spots with reads above zero. Thus, we calculated the NZRSCD to obtain a measure of the frequency of spots with reads above zero and derived a gene rank by calculation the average of ZFCMD and NZRSCD.

Genes with a rank-score below the median of the observed rank-scores were removed from the preliminary gene list. The filtered gene list was analyzed for enriched gene ontologies (GO) using the GOATOOLS python package [63] showing enrichment of immune and chemokine related GOs (chemokine activity, chemokine-mediated signaling pathway, antimicrobial humoral immune response mediated by antimicrobial peptide, inflammatory response). Thus, we added all chemokines observed in the ST data to the preliminary list and re-ran the filtering to obtain the final filtered gene list. The Relapse signature was derived from this list by accumulating all genes that were unanimously up- or downregulated in all spot classes. The NAG signature was derived by accumulating genes that were exclusively up- or downregulated in relapse in NCG spots.

Receptor-Ligand Interaction Analysis of Chemokines of Relapse and NAG signature

To investigate what receptors are present and might act as receivers of the chemokines observed in the Relapse and NAG sigantures squidpy's v1.2.3 [64] implementation of the CellPhoneDB algorithm [65] was applied to the normalized and scaled but non-logarithm transformed (see section Identification of Relapse and Normal Appearing Gland (NAG) signatures) ST data. Omnipath [66] interactions were limited to "receptor" for the receiver and "ligand" transmitter and filtered to include only entries with at least one published reference. The histopathology classes assigned to the ST spots were used as cluster-key and permutation test was run with 1000 permutations and threshold of 0.01 for required cells per cluster. Values were calculated for each core individually and corresponding interactions were subsequently combined by calculating the mean of the mean-values or combining the p-values using Fisher's method. Not-a-number (NaN) p-values were omitted during combination. In case all p-values for one interaction were NaN, we set the respective p-value in the combined-result tables to 1. Results were visualized with squipy's plotting function.

Single-sample Gene Set Enrichment Analysis (ssGSEA) and score calculation

The ssGSEA approach is an in-house implementation of the algorithm presented by Markert et al. [13], which has also been used in a previous study by us on PCa samples[14]. To handle the sparsity challenge in ST data for ssGSEA, gene expression values were centered by subtracting the mean value for each gene before sorting. This will ensure that genes with zero expression in one sample will get a lower rank if it is highly expressed in other samples, compared to genes with zero or low expression across all samples. Scores were calculated separately for up- and downregulated parts of the Relapse and NAG signatures and combined by calculating the mean of the up- and negated downregulated ssGSEA scores. All ssGSEA scores were min-max scaled to a range between -1000 and 1000. Significant scores were determined by calculating a distribution of scores for n=1000 unique permutations of random gene rankings. One-sided p-values for each sample/spot score were calculated from this distribution and combined for up- and downregulated part using Fisher's method. ST spot scores were considered significant when p-values <= 0.05/number of signature genes ($p_{Relapse}$ <= 0.001, p_{NAG} <= 0.003) and an absolute score > 200. For bulk samples a p-values <= 0.05 and an absolute score > 200 was considered significant.

Metabolite detection with MALDI-MSI

Serial tissue sections from the same 32 samples that were used for ST were placed on conductive slides and analyzed with MALDI time-of-flight (TOF) MSI for the spatial detection of small metabolites and lipids. Prior to MSI, the sections were sprayed with matrix using the HTX TM-Sprayer™ system (HTX Technology). The matrix solution consisted of 7 mg/mL *N*-(1-naphthyl) ethylenediamine dihydrochloride (NEDC) in 70% methanol. Spraying parameters included 18 layers with 0.06 ml/min flow rate and 1200 mm/min nozzle velocity, 3 mm track spacing, 10 psi pressure, 2 l/min gas flow rate, 40 mm nozzle height, 75°C nozzle spray temperature and 35°C plate temperature. Following matrix application, MSI was performed with a rapifleX™ MALDI TissuetyperTM (Bruker Daltonics) equipped with a 10 kHz laser shooting 200 shots per pixel at a 10 kHz frequency. Negative ion mode was used with a mass range of m/z 80-1000 and a spatial resolution of 30 µm. After MSI, the matrix-covered tissue sections were stored dry and dark at room temperature until HES staining was performed within 2 weeks. Metabolites were identified by MS/MS and accurate masses from our previous study using the same methods for equivalent PCa samples [67]. Zinc was detected as an adduct with chloride ($ZnCl_3^-$) and was previously identified by its isotopic pattern [11].

Integration of ST and MALDI-MSI data

MALDI-MSI data were binned/down sampled to 80% of its original datapoints in FlexImaging (Version 5.0, Bruker Daltonics) and further baseline corrected (top-hat) and root-mean square (RMS) normalized using SCILS lab Pro (Version 2024a, Bruker Daltonics). Ion images of identified metabolites (intensity given by max peak height) were exported to imzML files and co-registered to ST data using an in house develop method (publication in preparation).

HRMAS NMR Metabolomics

NOESY HRMAS NMR data was collected as previously described on a 600 MHz Bruker Avance III NMR spectrometer equipped with a magic angle spinning (MAS), ^{1}H / ^{13}C probehead (Bruker Biospin) [10]. After automics phase [68] and baseline correction, spectra were probabilistic quotient normalized [69], aligned with icoshift [70] and ppm ranges specific for the respective metabolites (succinate: 2.415-2.395, lactate: 4.15-4.08, citrate: 2.74-2.47, glutamate: 2.36-2.305, taurine: 3.445-3.37) numerically integrated using the trapezoidal rule. For each metabolite the raw integrals were min-max scaled.

Immunohistochemistry staining of LPS and LTA

To estimate bacterial infection/presence in the 32 ST samples we performed immunohistochemistry staining of neighboring 10 µm cryo-sections of lipopolysaccharides (LPS) and lipoteichoic acid (LTA). Cryo-sectioned tissue was fixed in 4% formalin for 15 min, washed twice in TBS-T at room temperature. Subsequently, peroxidases were blocked using 0.3% hydrogen peroxide followed by blocking of unspecific binding sites using in 10% normal serum with 1% BSA in TBS for 2 hours at room temperature. Primary antibodies against LPS and LTA (Abcam ab35654, Thermo MA1-7402) were used at 2,5 µg/ml and 2 µg/ml in TBS-T with 1 % BSA and incubated on tissue over night at 4°C. The tissue was washed twice in TBS-T prior incubation with secondary antibody (EnVision anti-mouse-HRP/DAB+ system, Agilent), 3,3'-Diaminobenzidine (DAB) development, counterstaining with hematoxylin, dehydration, and mounting were done according to manufacturer's recommendations. Stained tissues were scanned on an Olympus VS200 ASW 3.3 (Build 24382) slide scanner in bright field at 40x magnification resulting in a resolution of 136,866 nm/pixel. Images were processed with QuPath using building functions for cell detection to obtain mean DAB stain intensity per cell. HE images of the ST data were registered onto corresponding DAB-stained images using affine transformation derived from 3 manually determined corresponding points for each image pair. For both Relapse and NAG

signature, we calculated inverse-distance interpolated activity values for each cell center using the transformed ST-spot coordinates and signature activity as input (using k-dimensional tree, KDTree from python package SciPy, leafsize=10, use 8 nearest data points, eps=0.1)

Subclassification in 10 spot-subsets

Based on the classification of patients (relapse/no relapse), samples (cancer/field effect/normal) and spots (cancer, stroma, NCG) we classified spots into 10 groups. The spot-groups were defined by having combination of classifications, for example, relapse cancer NCG were defined as all normal appearing gland spots from Cancer samples in relapsing patients, while no relapse normal stroma was defined as all stroma spots from normal samples in non-relapsing patients. In this setup cancer spots were not distinguished by ISUP grade. In addition, NCG spots from both cancer and field effect samples were merged into similar groups. Thus, for example, the relapse cancer NCG group contained gland spots from relapsing patients from both cancer and field effect samples. Spots classified as (lymphocyte-enriched stroma, PNI, and others) were excluded from these spot-groups.

Validation of prognostic power of Relapse and NAG signatures in public data and comparison with prostate-related gene sets

We used 41 prostate-related gene sets selected from various sources [8, 9, 12, 14] in addition to our Relapse and NAG signatures for the ssGSEA analysis to evaluate prognostic power and relation to biological processes in the prostate of Relapse and NAG signatures (details in Supplementary Table S2). We used 38 of these gene sets for analysis in our ST and public data, and three additional gene sets for analysis only in public data (Supplementary Table S2 and S3). The three additional gene sets were made by genes for three commercially available gene signatures for aggressive PCa, CCP, GPS and Decipher [71]. For these three, we used only the selection of genes from these signatures and not the scoring algorithms for scoring the signatures in clinical samples.

Prostate specific-cell type and immune-cell genes downloaded from Joseph et al 2021 (Supplementary Table S3 and S8) [9] contained genes enriched in 5 prostate-specific cell types, and prostate-specific enrichment of genes in 19 immune-cell types. To created prostate-specific cell type gene sets from these 24 cell types, we ranked the genes for each cell type by q-value (ascending) and fold-change (descending). The genes were sorted by the average rank over q-value and fold-change, and the top 75 ranked genes were selected to create a gene set for each cell type. We further validated each of the 19 immune-cell type gene sets with 142 corresponding immune gene sets downloaded from Azimuth (https://azimuth.hubmapconsortium.org/) [72], for PBMC (Peripheral Blood Mononuclear Cells) version 1-3, and Bone Marrow version 1 and 2. Each gene set from Azimuth contained 10 genes. We used GSEA [13] to score each of the 164 Azimuth gene sets in the 19 ranked immune gene sets from Joseph et al. [9], and then evaluated whether gene sets from Azimuth were enriched in our gene sets generated from Jospeh et al. [9] The results generally showed enrichment of Azimuth immune gene sets with corresponding immune gene sets from Joseph et al., demonstrating that the gene sets downloaded from Joseph et al. represented their respective immune cell-types well. Two exceptions were CD4+ Naïve and CD8+ Naïve signatures which showed a more general enrichment in various CD4+ and CD8+ cells from Azimuth. The validation was also not able to distinguish subtypes of immune cells, for example different Dendritic subtypes (EREG, IGSF21, and TREM2), Basophil-Mast 1 and 2, Classical and Nonclassical Monocyte, and Natural Killer and Natural Killer T cells.

To compare these 41 gene sets and evaluate prognostic power and relation to biological processes in the prostate of our Relapse and NAG signatures in public data, we calculated ssGSEA scores for all gene sets in all 2512 samples from 12 public datasets (Supplementary Table S3). The public data gene expression values were not centered before ssGSEA analysis. Correlations between gene sets in each

dataset were calculated by Pearson correlation. The overall correlation for two gene sets was calculated as the average correlation over all 12 datasets. Complete tables with correlations for all gene sets in each individual dataset are given in Supplementary File 2**.**

Acknowledgement

This research was funded by the European Research Council (ERC) under the European Union's Horizon 2020 research and innovation program (grant agreement no. 758306), Norwegian University of Science and Technology (NTNU), the Liaison Committee between the Central Norway Regional Health Authority (RHA) and NTNU, the Norwegian Cancer Society and Terje Eugen Johnsen funds. All tissue samples were collected and stored by Biobank1, St. Olav's Hospital. Tissue sectioning, staining and scanning were performed by or in collaboration with the Histology lab at the Cellular & Molecular Imaging Core Facility (CMIC) at NTNU. The authors thank Ingunn Nervik, Kathrin Juanita Gravvold Torseth, and Borgny Ytterhus for excellent technical assistance during these experiments. Biobank1 performed isolation of RNA before bulk analysis. Transcriptomics experiments were carried out at the Genomics Core Facility at NTNU. MALDI MSI acquisitions were achieved using instrumentation at the MR Core facility, NTNU.

Alfonso Urbanucci wishes to thank the Academy of Finland project no. 349314; Cancer Foundation Finland; Norwegian Cancer Society project no. 198016-2018 & project no. 333723-2023, Tampere Institute for Advanced Study.

Competing interests: The authors declare no competing interests.

References

1. Pernar, C.H., et al., *The epidemiology of prostate cancer.* Cold Spring Harbor perspectives in medicine, 2018: p. a030361.
2. Haffner, M.C., et al., *Genomic and phenotypic heterogeneity in prostate cancer.* Nat Rev Urol, 2021. **18**(2): p. 79-92.
3. Shore, N.D., et al., *Biochemical recurrence in patients with prostate cancer after primary definitive therapy: treatment based on risk stratification.* Prostate Cancer Prostatic Dis, 2023.
4. Song, H., et al., *Single-cell analysis of human primary prostate cancer reveals the heterogeneity of tumor-associated epithelial cell states.* Nat Commun, 2022. **13**(1): p. 141.
5. Hirz, T., et al., *Dissecting the immune suppressive human prostate tumor microenvironment via integrated single-cell and spatial transcriptomic analyses.* Nat Commun, 2023. **14**(1): p. 663.
6. Berglund, E., et al., *Spatial maps of prostate cancer transcriptomes reveal an unexplored landscape of heterogeneity.* Nat Commun, 2018. **9**(1): p. 2419.
7. Erickson, A., et al., *Spatially resolved clonal copy number alterations in benign and malignant tissue.* Nature, 2022. **608**(7922): p. 360-367.
8. Henry, G.H., et al., *A Cellular Anatomy of the Normal Adult Human Prostate and Prostatic Urethra.* Cell Rep, 2018. **25**(12): p. 3530-3542 e5.
9. Joseph, D.B., et al., *Single-cell analysis of mouse and human prostate reveals novel fibroblasts with specialized distribution and microenvironment interactions.* J Pathol, 2021. **255**(2): p. 141-154.
10. Giskeodegard, G.F., et al., *Spermine and citrate as metabolic biomarkers for assessing prostate cancer aggressiveness.* PLoS One, 2013. **8**(4): p. e62375.
11. Andersen, M.K., et al., *Simultaneous Detection of Zinc and Its Pathway Metabolites Using MALDI MS Imaging of Prostate Tissue.* Anal Chem, 2020. **92**(4): p. 3171-3179.
12. Tessem, M.B., et al., *A Balanced Tissue Composition Reveals New Metabolic and Gene Expression Markers in Prostate Cancer.* PLoS One, 2016. **11**(4): p. e0153727.
13. Markert, E.K., et al., *Molecular classification of prostate cancer using curated expression signatures.* Proc Natl Acad Sci U S A, 2011. **108**(52): p. 21276-81.
14. Rye, M.B., et al., *The genes controlling normal function of citrate and spermine secretion are lost in aggressive prostate cancer and prostate model systems.* iScience, 2022. **25**(6): p. 104451.

15. Montironi, R., et al., *Subtle morphological and molecular changes in normal-looking epithelium in prostates with prostatic intraepithelial neoplasia or cancer.* Eur Urol, 1999. **35**(5-6): p. 468-73.
16. Ananthanarayanan, V., et al., *Alteration of proliferation and apoptotic markers in normal and premalignant tissue associated with prostate cancer.* BMC Cancer, 2006. **6**: p. 73.
17. Andersson, A., et al., *Single-cell and spatial transcriptomics enables probabilistic inference of cell type topography.* Commun Biol, 2020. **3**(1): p. 565.
18. Montoro, D.T., et al., *A revised airway epithelial hierarchy includes CFTR-expressing ionocytes.* Nature, 2018. **560**(7718): p. 319-324.
19. Joseph, D.B., et al., *Urethral luminal epithelia are castration-insensitive cells of the proximal prostate.* Prostate, 2020. **80**(11): p. 872-884.
20. Huang, F.W., et al., *Club-like cells in proliferative inflammatory atrophy of the prostate.* J Pathol, 2023. **261**(1): p. 85-95.
21. Joseph, D.B., et al., *5-Alpha reductase inhibitors induce a prostate luminal to club cell transition in human benign prostatic hyperplasia.* J Pathol, 2022. **256**(4): p. 427-441.
22. Karthaus, W.R., et al., *Regenerative potential of prostate luminal cells revealed by single-cell analysis.* Science, 2020. **368**(6490): p. 497-505.
23. Germanos, A.A., et al., *Defining cellular population dynamics at single-cell resolution during prostate cancer progression.* Elife, 2022. **11**.
24. Tang, S., et al., *Evidence that arachidonate 15-lipoxygenase 2 is a negative cell cycle regulator in normal prostate epithelial cells.* J Biol Chem, 2002. **277**(18): p. 16189-201.
25. Sorensen, K.D., et al., *Prognostic significance of aberrantly silenced ANPEP expression in prostate cancer.* Br J Cancer, 2013. **108**(2): p. 420-8.
26. Nunes-Xavier, C.E., et al., *The role of protein tyrosine phosphatases in prostate cancer biology.* Biochim Biophys Acta Mol Cell Res, 2019. **1866**(1): p. 102-113.
27. Zhang, Y., et al., *NCAPD3 exerts tumor-promoting effects in prostatic cancer via dual impact on miR-30a-5p by STAT3-MALAT1 and MYC.* Cell Death Discov, 2024. **10**(1): p. 159.
28. Lapointe, J., et al., *hCAP-D3 expression marks a prostate cancer subtype with favorable clinical behavior and androgen signaling signature.* Am J Surg Pathol, 2008. **32**(2): p. 205-9.
29. Mitra, R. and O.B. Goodman, Jr., *CYP3A5 regulates prostate cancer cell growth by facilitating nuclear translocation of AR.* Prostate, 2015. **75**(5): p. 527-38.
30. Owe-Larsson, M., et al., *The Role of Cocaine- and Amphetamine-Regulated Transcript (CART) in Cancer: A Systematic Review.* Int J Mol Sci, 2023. **24**(12).
31. Rostami, M.R., et al., *Smoking shifts human small airway epithelium club cells toward a lesser differentiated population.* NPJ Genom Med, 2021. **6**(1): p. 73.
32. Sokol, C.L. and A.D. Luster, *The chemokine system in innate immunity.* Cold Spring Harb Perspect Biol, 2015. **7**(5).
33. Ozga, A.J., M.T. Chow, and A.D. Luster, *Chemokines and the immune response to cancer.* Immunity, 2021. **54**(5): p. 859-874.
34. de Carvalho, G.B. and G.B. de Carvalho, *Duffy Blood Group System and the malaria adaptation process in humans.* Rev Bras Hematol Hemoter, 2011. **33**(1): p. 55-64.
35. Crawford, K.S. and B.F. Volkman, *Prospects for targeting ACKR1 in cancer and other diseases.* Front Immunol, 2023. **14**: p. 1111960.
36. Elson, J.K., et al., *The Duffy Antigen/Receptor for Chemokines (DARC) and prostate-cancer risk among Jamaican men.* J Immigr Minor Health, 2011. **13**(1): p. 36-41.
37. Nemesure, B., et al., *Distribution of Duffy Antigen Receptor for Chemokines (DARC) and Risk of Prostate Cancer in Barbados, West Indies.* J Immigr Minor Health, 2015. **17**(3): p. 679-83.
38. Shen, H., et al., *The Duffy antigen/receptor for chemokines (DARC) regulates prostate tumor growth.* FASEB J, 2006. **20**(1): p. 59-64.
39. Massara, M., et al., *Atypical chemokine receptors in cancer: friends or foes?* J Leukoc Biol, 2016. **99**(6): p. 927-33.
40. Mortier, A., et al., *CD26/dipeptidylpeptidase IV-chemokine interactions: double-edged regulation of inflammation and tumor biology.* J Leukoc Biol, 2016. **99**(6): p. 955-69.
41. Proost, P., et al., *Proteolytic processing of CXCL11 by CD13/aminopeptidase N impairs CXCR3 and CXCR7 binding and signaling and reduces lymphocyte and endothelial cell migration.* Blood, 2007. **110**(1): p. 37-44.
42. Karami, A.A., et al., *Detection of bacterial agents causing prostate infection by culture and molecular methods from biopsy specimens.* Iran J Microbiol, 2022. **14**(2): p. 161-167.
43. Chatterjee, A., et al., *Validation of Prostate Tissue Composition by Using Hybrid Multidimensional MRI: Correlation with Histologic Findings.* Radiology, 2022. **302**(2): p. 368-377.
44. Ahmad, F., M.K. Cherukuri, and P.L. Choyke, *Metabolic reprogramming in prostate cancer.* Br J Cancer, 2021. **125**(9): p. 1185-1196.
45. Costello, L.C. and R.B. Franklin, *A comprehensive review of the role of zinc in normal prostate function and metabolism; and its implications in prostate cancer.* Arch Biochem Biophys, 2016. **611**: p. 100-112.
46. Schiliro, C. and B.L. Firestein, *Mechanisms of Metabolic Reprogramming in Cancer Cells Supporting Enhanced Growth and Proliferation.* Cells, 2021. **10**(5).

47. Gaber, T., C. Strehl, and F. Buttgereit, *Metabolic regulation of inflammation.* Nat Rev Rheumatol, 2017. **13**(5): p. 267-279.
48. Persson, B.E. and G. Ronquist, *Evidence for a mechanistic association between nonbacterial prostatitis and levels of urate and creatinine in expressed prostatic secretion.* J Urol, 1996. **155**(3): p. 958-60.
49. McNaughton, C.O. and T. Wilt, *Allopurinol for chronic prostatitis.* Cochrane Database Syst Rev, 2002(4): p. CD001041.
50. Motrich, R.D., et al., *Uric acid crystals in the semen of a patient with symptoms of chronic prostatitis.* Fertil Steril, 2006. **85**(3): p. 751 e1-751 e4.
51. De Marzo, A.M., et al., *Inflammation in prostate carcinogenesis.* Nat Rev Cancer, 2007. **7**(4): p. 256-69.
52. Song, X., et al., *Effect of taurine on the proliferation, apoptosis and MST1/Hippo signaling in prostate cancer cells.* Transl Cancer Res, 2022. **11**(6): p. 1705-1712.
53. Baliou, S., et al., *Protective role of taurine against oxidative stress (Review).* Mol Med Rep, 2021. **24**(2).
54. Andersen, M.K., et al., *Integrative metabolic and transcriptomic profiling of prostate cancer tissue containing reactive stroma.* Sci Rep, 2018. **8**(1): p. 14269.
55. Giafaglione, J.M., et al., *Prostate lineage-specific metabolism governs luminal differentiation and response to antiandrogen treatment.* Nat Cell Biol, 2023. **25**(12): p. 1821-1832.
56. Bertilsson, H., et al., *A new method to provide a fresh frozen prostate slice suitable for gene expression study and MR spectroscopy.* Prostate, 2011. **71**(5): p. 461-9.
57. Andersen, M.K., et al., *Sample Preparation for Metabolite Detection in Mass Spectrometry Imaging.* Methods Mol Biol, 2023. **2688**: p. 135-146.
58. Andersen, M.K., et al., *Spatial transcriptomics reveals strong association between SFRP4 and extracellular matrix remodeling in prostate cancer.* Research Square, 2023.
59. Bankhead, P., et al., *QuPath: Open source software for digital pathology image analysis.* Sci Rep, 2017. **7**(1): p. 16878.
60. Epstein, J.I., et al., *Contemporary Gleason Grading of Prostatic Carcinoma: An Update With Discussion on Practical Issues to Implement the 2014 International Society of Urological Pathology (ISUP) Consensus Conference on Gleason Grading of Prostatic Carcinoma.* Am J Surg Pathol, 2017. **41**(4): p. e1-e7.
61. Wolf, F.A., P. Angerer, and F.J. Theis, *SCANPY: large-scale single-cell gene expression data analysis.* Genome Biol, 2018. **19**(1): p. 15.
62. Satija, R., et al., *Spatial reconstruction of single-cell gene expression data.* Nat Biotechnol, 2015. **33**(5): p. 495-502.
63. Klopfenstein, D.V., et al., *GOATOOLS: A Python library for Gene Ontology analyses.* Sci Rep, 2018. **8**(1): p. 10872.
64. Palla, G., et al., *Squidpy: a scalable framework for spatial omics analysis.* Nat Methods, 2022. **19**(2): p. 171-178.
65. Efremova, M., et al., *CellPhoneDB: inferring cell-cell communication from combined expression of multi-subunit ligand-receptor complexes.* Nat Protoc, 2020. **15**(4): p. 1484-1506.
66. Turei, D., T. Korcsmaros, and J. Saez-Rodriguez, *OmniPath: guidelines and gateway for literature-curated signaling pathway resources.* Nat Methods, 2016. **13**(12): p. 966-967.
67. Andersen, M.K., et al., *Spatial differentiation of metabolism in prostate cancer tissue by MALDI-TOF MSI.* Cancer Metab, 2021. **9**(1): p. 9.
68. Wang, T., et al., *Automics: an integrated platform for NMR-based metabonomics spectral processing and data analysis.* BMC Bioinformatics, 2009. **10**: p. 83.
69. Dieterle, F., et al., *Probabilistic quotient normalization as robust method to account for dilution of complex biological mixtures. Application in 1H NMR metabonomics.* Anal Chem, 2006. **78**(13): p. 4281-90.
70. Savorani, F., G. Tomasi, and S.B. Engelsen, *icoshift: A versatile tool for the rapid alignment of 1D NMR spectra.* J Magn Reson, 2010. **202**(2): p. 190-202.
71. Na, R., et al., *Clinically available RNA profiling tests of prostate tumors: utility and comparison.* Asian J Androl, 2016. **18**(4): p. 575-9.
72. Hao, Y., et al., *Integrated analysis of multimodal single-cell data.* Cell, 2021. **184**(13): p. 3573-3587 e29.